Geophysical Journal International

Geophys. J. Int. (2013) **193,** 747–762 doi: 10.1093/gji/ggs133

Shallow water waves generated by subaerial solid landslides

S. Viroulet,[1] D. Cébron,[2] O. Kimmoun[1,3] and C. Kharif[1,3]

[1] *CNRS and Aix-Marseille University, IRPHE (UMR* 7342*),* 13384*, Marseille cedex* 13*, France. E-mail: viroulet@irphe.univ-mrs.fr*
[2] *Institut für Geophysik, ETH Zürich, Sonneggstrasse* 5, *Zürich,* CH-8092, *Switzerland*
[3] *Ecole Centrale Marseille,* 13451, *Marseille cedex* 20, *France*

Accepted 2012 December 30. Received 2012 December 3; in original form 2012 July 20

SUMMARY

Subaerial landslides are common events, which may generate very large water waves. The numerical modelling and simulation of these events are thus of primary interest for forecasting and mitigation of tsunami disasters. In this paper, we aim at describing these extreme events using a simplified shallow water model to derive relevant scaling laws. To cope with the problem, two different numerical codes are employed: one, SPHysics, is based on a Lagrangian meshless approach to accurately describe the impact stage whereas the other, Gerris, based on a two-phase finite-volume method is used to study the propagation of the wave. To validate Gerris for this very particular problem, two numerical cases of the literature are reproduced: a vertical sinking box and a 2-D wedge sliding down a slope. Then, to get insights into the problem of subaerial landslide-generated tsunamis and to further validate the codes for this case of landslides, a series of experiments is conducted in a water wave tank and successfully compared with the results of both codes. Based on a simplified approach, we derive different scaling laws in excellent agreement with the experiments and numerical simulations.

Key words: Tsunamis; Submarine landslides; Impact phenomena; Volcanic hazards and risks.

1 INTRODUCTION

Tsunami waves are generated by various geophysical events, such as earthquakes, volcano flank collapses, asteroid impacts or submarine and subaerial landslides. These physical mechanisms of generation of tsunami waves are reported in the book of Levin & Nosov (2009). The most frequent causes of tsunamis are underwater earthquakes due to sudden changes in the seafloor (Grilli *et al.* 2007; Popinet 2011) and these cases are thus widely studied in the literature. For the cases of tsunami waves generated by volcano flank collapses, asteroid impacts or submarine and subaerial landslides one can refer to the papers by McMurtry *et al.* (2004), Kharif & Pelinovsky (2005) and Assier-Rzadkieaicz *et al.* (2000), respectively. Tsunamis generated by landslides are rarer but can be locally more dangerous because they form near the coast and sometimes may generate so-called mega-tsunamis, which are characterized by localized extreme run-up heights leading to a significant hazard for the population [Lituya Bay 1958, Alaska, (Fritz *et al.* 2009), Spirit Lake 1980, Washington USA (Glicken *et al.* 1989) and maybe Cumbre Vieja, Canary Islands, (Ward & Day 2001; Lovholt *et al.* 2008; Abadie *et al.* 2012)]. However, modelling the landslide motion remains challenging because the interactions between the slide and the water as well as the influence of the rheology are difficult to capture as we will see below. In addition, the time evolution of the associated waves remains intricate to forecast.

Previous studies on submarine and subaerial landslides (see Fig. 1 for the classification) tried to understand the influence of the landslide parameters on the generated waves. Murty (1979) analytically calculated the wave height generated by a submarine landslide, assuming that the potential energy of the slide was transferred in a solitary wave. Pelinovsky & Poplavsky (1996) and Watts (1997) calculated analytically the final velocity of a submerged solid sliding down a slope. Sammarco & Renzi (2008) developed a two-horizontal-dimension analytical model to study the generation and propagation of landslide-induced tsunami along a plane beach. Didenkulova *et al.* (2010) studied the generation and propagation of tsunami waves generated by submarine landslide of variable volume in a basin of variable depth. They concluded that the amplitude of the wave varies non-monotonically with the distance. Experimental investigations were carried out using solid bodies: Law & Brebner (1968) used a solid box to generated subaerial landslides, they concluded that the leading wave is always the most significant. Kamphuis & Bowering (1972) used a tray rolling down a roller ramp. They observed that the main parameters to evaluate the wave height was the Froude number for the impact velocity and the slide volume. Based on their experiments using solid bodies, Walder *et al.* (2003) demonstrated that the shape and the height of the generated wave in near field depend on the water depth, the volume of the slide and the duration of the submerged landslide motion. Enet *et al.* (2007) performed experiments dealing with 3-D rigid underwater landslides. They observed that the slide initial acceleration is an important parameter for the tsunami generation. Experiments with granular materials were conducted to study the influence of the slide rigidity. Fritz (2002) used a pneumatic

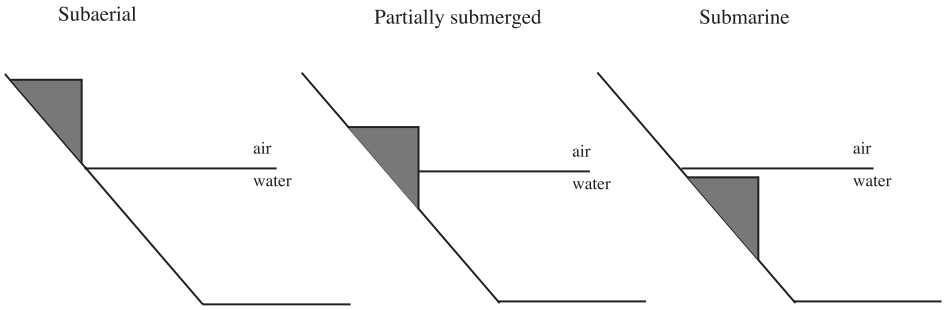

Figure 1. Landslide generated tsunami waves classification. This classification is based on the initial position of the landslide: subaerial, partially submerged or submarine.

landslide generator to study subaerial landslide impacts with Froude number $Fr > 1$. A particle image velocimetry (PIV) method were used to analyse the interactions between the slide and water (Fritz *et al.* 2003a,b). From all these experiments, predictive equations on wave amplitude, wave period, wavelength and propagation velocity were provided using multiple regressions with very good correlation coefficients. An extension to 3-D cases was performed by Mohammed & Fritz (2012). Ataie-Ashtiani & Nik-Khah (2008) performed laboratory experiments on impulse waves generated by rigid and deformable slide masses. They showed that the maximum wave crest amplitude is strongly affected by the landslide impact velocity, thickness, deformation and weakly affected by the shape. Several numerical methods were used to understand and analyse these observations. Heinrich *et al.* (2001) used non-linear shallow water equations to model fluid and slide motions. However, landslide tsunami waves may be more dispersive than tectonic ones and strong vertical accelerations may occur when the slide impacts water so the usual assumptions for equations (no vertical acceleration and non-dispersive waves) are not valid. Using potential flow numerical methods, like the boundary elements method (BEM) used by Grilli *et al.* (2002), correctly simulate tsunami waves generated by submarine landslide. However, the strong vorticity and the possible fragmentation of the free surface produced by a subaerial landslide raise numerical issues with this method. Monaghan & Kos (2000) used the smoothed particle hydrodynamics (SPH) to simulate the interactions between sliding masses and water for subaerial cases. These single-phase flow simulations reproduce successfully some challenging features, like the reverse plunging breaking and a dimensional analysis were performed on the amplitude of the wave assuming like Murty (1979) that the potential energy of the weighted box is transferred in the generated solitary wave.

Liu *et al.* (2005) used a finite-volume discretization and a volume-of-fluids (VOF) method to numerically reproduce their experiments of run-up and rundown generated by 3-D sliding masses. They showed that the run-up is significantly larger for subaerial landslides and that the run-up and rundown are controlled by the size, the initial submergence and the motion of the slide. Heinrich (1992) used a finite difference technique to solve incompressible Navier–Stokes equations for the simulation of submarine and subaerial landslides. More recently, Fernandez-Nieto *et al.* (2008) used a Savage–Hutter type model to describe both deformed landslide and associated waves. Abadie *et al.* (2010) considered a multiple-fluid Navier-Stokes model using a finite volume discretization and a VOF method to track the interface and describe the interactions between slide/air/water. A more detailed presentation of numerical methods used to simulate tsunami waves can be found in Abadie *et al.* (2010).

In this work, we perform 2-D experiments in a 18-m-long, 0.65-m-wide and 1.5-m-high wave tank with a solid body sliding down a slope with constant water depths. To study the influence of the main parameters of a solid landslide generating waves, the initial mass and position of the solid are modified to create subaerial landslides. We numerically reproduce the experiments using two codes: Gerris, a tree-based adaptive solver using a finite-volume discretization and a VOF method to track the interface (Popinet 2003, 2009) and SPHysics (Gómez-Gesteira *et al.* 2012a,b), a lagrangian meshless method. Based on these results, additional numerical experiments were performed to systematically study the influence of solid velocity, slope angle, initial water depth and shape of the solid on the generated water waves in the near and far field.

The main objective of this work is twofold: (i) validation of both codes on the time evolution of the free-surface elevation and (ii) elaboration of a simplified model for prediction of wave generation and propagation as a function of the initial configuration of subaerial solid landslides. The experimental and numerical studies of subaerial landslide generated waves are presented in Section 2. Scaling laws on the maximum amplitude arrival time and on the maximum amplitude evolution are derived in Sections 3 and 4, respectively, and then validated by comparison with our experiments.

2 EXPERIMENTAL VALIDATION ON WAVE GENERATED BY SUBAERIAL SOLID LANDSLIDE

Several experiments involving subaerial solid landslides are performed varying some parameters like the water depth, the mass and the initial position of the solid. Based on these experiments, a cross validation of both numerical methods (SPHysics and Gerris) can be performed in near and far fields, respectively.

2.1 Experimental set-up and data acquisition

Experiments are conducted at École Centrale de Marseille in a 18-m-long, 0.65-m-wide and 1.5-m-high wave tank. A plane slope is installed on one side of the flume and an absorbing beach on the other side. The slope is made of a polyvinyl plate of 1.5 cm thickness, 2.2 m length and 0.65 m width, fixed on the left boundary with 35° inclination. The water depth is fixed to 0.43 and 0.38 m, respectively (see Fig. 2). The wedge used to generate the impulse wave is represented by a box with a front angle $\theta = 45°$. To avoid water to pass over the solid, an other 1-m-long, 0.65-m-wide and 1.0-cm-thick polyvinyl plate is fixed on the front of the box. An aluminum rod is screwed to the top of the plate and the base of the solid to avoid elastic flexion. The solid slides down the slope by gravity rolling on four wheels. The gap between the solid and the slope is about 1 cm (radius of the wheels). To reduce this clearance,

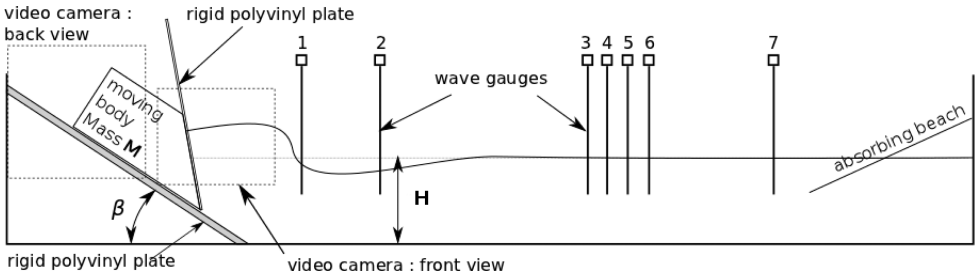

Figure 2. Schematic view of the experimental set up for subaerial landslide generated waves. Wave gauges are located at 1.80 m, 2.805 m, 4.98 m, 5.16 m, 5.34 m, 5.70 m and 10.08 m from the intersection of the slope with the bottom of the flume (not to scale).

we place the polyvinyl plate approximately 1 mm above the slope. This small gap is supposed to have very few effects on the generated waves and is thus neglected in our numerical simulations. The sides of the tank are made of transparent glass, which allows the use of two cameras to follow the time evolution of the free surface. The displacement of the solid is filmed by one of the cameras at 100 fps (back view on Fig. 2), the other one is installed perpendicular to the side of the tank at the same level as the undisturbed free surface, to follow the impact with water at 1000 fps (front view on Fig. 2). The recorded pictures are only used to compare qualitatively the overall behaviour of the free surface with the numerical simulations. The propagation and the amplitude of the generated waves are measured using seven electrical contact-type gauges installed along the wave tank at 1.80, 2.805, 4.98, 5.16, 5.34, 5.70 and 10.08 m, respectively, from the intersection of the slope with the bottom of the flume. They are all located at the same distance from the transparent sides assuming the propagation to be unidimensional along the flume width [this has been confirmed by Heinrich (1992) in a similar wave tank configuration]. Several experiments are conducted changing the water depth, mass and initial position of the solid. A high position of the solid corresponds to a subaerial landslide whereas a low position of the solid corresponds to a partially submerged landslide. In both cases, the front of the solid impacts the undisturbed free surface non-perpendicularly (with a 10° angle). In the remainder of the paper, these two configurations are called high and low positions.

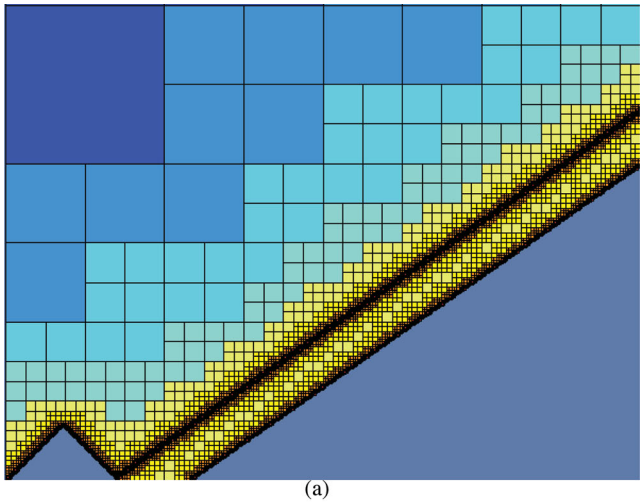

Figure 3. (a) Representation of the domain configuration and initial adaptive mesh refinement on the free surface. The discretization is organized hierarchically as a quadtree with a root cell (dark blue) and leaf cell (dark red) (Popinet 2003). (b) Free-surface elevation given by SPHYSICS[2] for three different models of viscosity: the artificial viscosity (Monaghan 1992), the laminar stress approach (Lo & Shao 2002) and the use of a subparticle scale (SPS) approach (Dalrymple & Rogers 2006). The excellent agreement shows that the results of the flow considered in this work do not depend on the choice of the viscosity model.

2.2 Numerical methods for our 2-D simulations

The code Gerris is a tree-based adaptive solver using a finite-volume discretization and a VOF method to track the interface (Popinet 2003, 2009, see also the appendix for further details). The computational domain used is defined by a 12 m × 12 m square. The mesh refinement is controlled by the interface position and the vorticity field. The code automatically adapts the refinement on the free surface and the generated vorticity. The finest level 11, leads to a smallest cell edge of about 6 mm ($12/2^{11}$) on the free surface and for the generated vorticity. We use the values of density and viscosity for air and water at ambient temperature of 20 °C and ambient pressure of 1013 hPa ($\rho_w = 1000\ \mathrm{kg\,m^{-3}}$, $\rho_a = 1.2\ \mathrm{kg\,m^{-3}}$, $\mu_w = 1.0 \times 10^{-6}\ \mathrm{kg\,m^{-1}\,s^{-1}}$ and $\mu_a = 1.8 \cdot 10^{-5}\ \mathrm{kg\,m^{-1}\,s^{-1}}$). To ensure the stability of the simulation for a large ratio of density, $\rho_w/\rho_a \approx 800$ in this case, we tune the solver by decreasing the tolerance corresponding to the maximum error allowed in local volume/mass conservation and by increasing the maximum number of iterations. Instead of numerically generating a slope and imposing a vertical and horizontal velocity to the solid, we choose to rotate anticlockwise all the domain and the gravity by an angle equal to 35° (see Fig. 3a). The curvilinear velocity of the solid is imposed (Dirichlet boundary condition on the velocity) and the slope is a boundary of the domain. This configuration is much easier to compute especially for the displacement of the solid. The boundary conditions are a free outflow at the top of the domain, which correspond to Neumann conditions on the velocity (the normal derivative

of the velocity is equal to zero on the boundary) and a Dirichlet condition on the pressure (fixed to zero). A no-slip condition is imposed at the bottom of the tank on the velocity and a symmetry condition is imposed on both sides of the domain, which is equivalent to a free-slip impermeable boundary. For the simulations considered in this work, the initial condition for the water and the air is systematically zero for the velocity.

The SPH code used in this study is the code SPHysics (see Cébron & Sigrist 2008; Gómez-Gesteira *et al.* 2010, 2012a,b, for details and validations). This code simulates single-phase flows with a free-surface and moving solids in the numerical domain. This means that the influence of the air flow is neglected in these simulations, which can lead to slightly enhanced wave heights. The parameters used are rather usual for these kind of computations: particles are moved using the XSPH variant (Monaghan 1989), the variable time step solver is a predictor–corrector solver and the smoothing kernel used is a cubic spline. The simulations presented in this work use a sound velocity of $40\sqrt{gH}$, and a number of particles between 10^5 and 3×10^5, depending on the considered flow, which leads to a CPU time between 2 days and several weeks on a standard workstation. A well-known problem in the SPH numerical method is the way the viscosity is taken into account in the fluid and along solid boundaries. For the boundary conditions, the so-called repulsive boundary conditions are used (Monaghan & Kos 2000; Rogers & Dalrymple 2008). Concerning the viscosity in the bulk of the fluid, three different methods exist, which are compared in Fig. 3(b). The artificial viscosity suggested by Monaghan (1992) is often used for its simplicity (squares, with an artificial viscosity coefficient $\alpha = 0.1$). Another way is to estimate the laminar stress term as in Lo & Shao (2002), which corresponds to the diamonds. In addition to this laminar viscosity, a subparticle scale (SPS) approach can be used (cross in Fig. 3b) for turbulent flows (Dalrymple & Rogers 2006). It is clear that these methods give the same results for the cases considered in this work. Hence, we choose to use the purely laminar stress approach (Lo & Shao 2002).

2.3 Experimental and numerical results

Comparisons between the experimental free-surface elevation and numerical wave profiles for both configurations are shown in Fig. 4. Wave breaking occurs for the higher position of the solid. This phenomenon is well described by SPH simulation. We can clearly observe the breaking of the wave which presents a flat backward face. Note that a lot of particles are needed to capture the breaking. Consequently, we define a reduced numerical wave tank to have a reasonable computational time. The free-surface elevation computed with Gerris has a smaller steepness and amplitude than in the experiment. We cannot clearly see the wave breaking, but oscillations at the crest of the wave (this phenomenon is also observed for higher resolutions). Within the framework of the low position of the solid, a good agreement between experimental data and numerical results is obtained for the free-surface elevation.

The velocity of the solid is directly imposed in the numerical simulations from the experimental records of its displacement along the slope. We measure the successive positions during the motion at a fixed time step (frame rate of the camera). These positions are interpolated by a polynomial representing the vertical displacement of the solid as a function of time (see Table 1).

Fig. 5 displays the experimental and numerical evolution of the free-surface elevation recorded at the first probe for both configurations [panel (a) low position, panel(b) high position]. For the lower configuration, the amplitude of the first crest is underestimated by the two codes. Nevertheless, the SPH method seems to

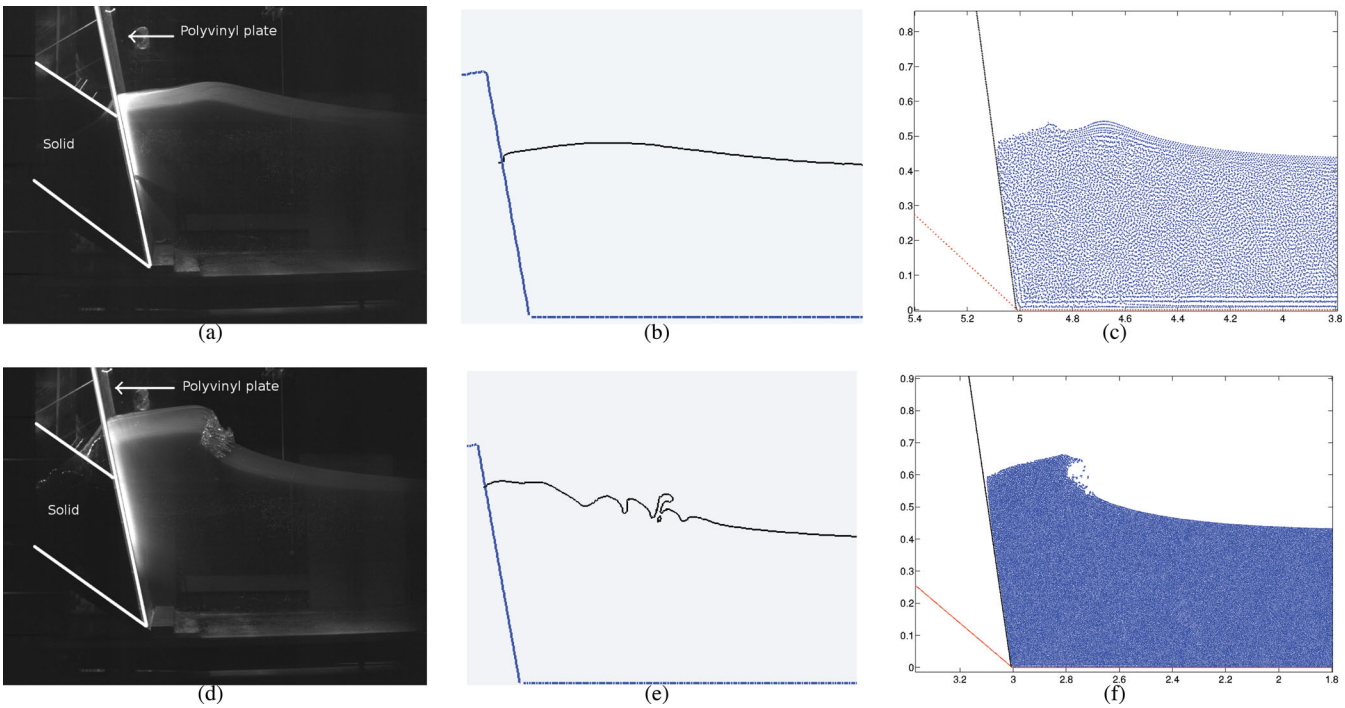

Figure 4. Comparison between the experiment and simulated free surface for both initial configurations: panel (a) low position, panel (d) high position when the solid reaches the bottom of the tank. Panels (b) and (c) correspond to Gerris and SPH results for low position, panels (e) and (f) for high position. SPH method seems to be more accurate than Gerris for the simulation of the impact. Oscillations on the free surface in panel (e) probably correspond to the wave breaking experimentally observed.

Table 1. Coefficients of the polynomial representing the vertical displacement of the solid as a function of time for both initial positions given by $P(t) = \sum_{n=2}^{n=7} a_n t^n$.

Coefficients	a_2	a_3	a_4	a_5	a_6	a_7
Low position	0.8515	2.241	−5.315	2.45	0	0
High position	−0.0976	19.3853	−73.0275	140.694	−140.3217	54.5643

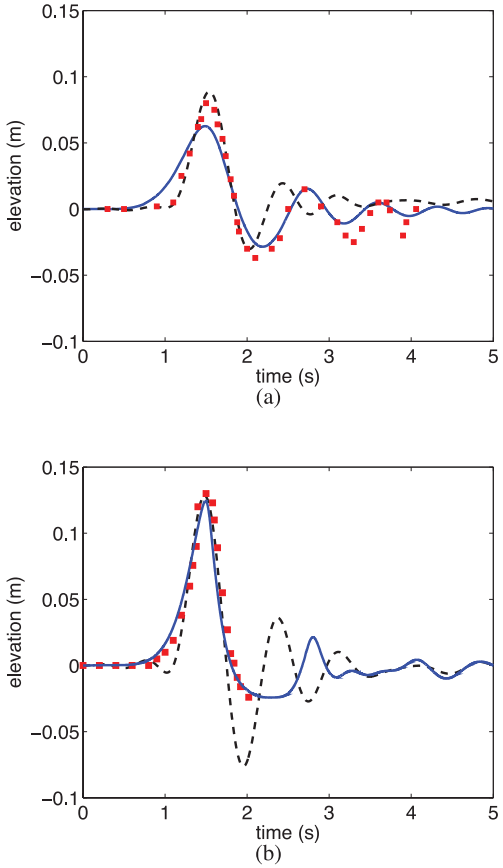

Figure 5. First probe located at 1.80 m from the intersection of the slope with the bottom of the tank. Comparison between experimental and computed waves (a) low position and (b) high position. Experiment (dashed line), Gerris (solid line) and SPH (□). Both numerical methods are in satisfactory agreement with the experiment.

be more accurate with only 5 per cent error, which is the relative deviation from experimental data. With Gerris, the most important discrepancy is the significantly lower crest in the simulation with a larger wavelength. The underestimated amplitude corresponds to a 20 per cent error. Following the first crest, the amplitude of the trough is correctly computed with Gerris, whereas the SPH method overestimates it with a 10 per cent error. Later in the simulation, the amplitude of the crest is correctly calculated with Gerris and SPH but the troughs are still overstimated and a weak time-lag occurs. Initial wave acceleration seems to be lower in the numerical simulations, the trough and the second crest reach the wave gauge later than in the experiment. For the highest configuration (Fig. 5b), the amplitude of the first crest is well computed by SPH and Gerris. The most important discrepancy occurs for the following crest and trough (see Fig. 5b).

Fig. 6 shows the time evolution of the elevation at probes 2 and 4 (2.805 and 5.16 m), respectively from the intersection of the slope with the bottom). The simulation is stopped when the first waves reach the boundary of the domain to avoid any reflection effect in the results. Due to the computational cost, the SPH domain length is smaller than the Gerris one, especially for the high position where a lot of particles are used (for the highest resolution for instance, the SPH domain length is 5 m). This naturally leads to a shorter time evolution in the simulation. For the low position of the solid the amplitude is still slightly underestimated at wave gauge 2 with Gerris. SPH simulation is in a satisfactory agreement with the experiment. For both numerical methods, the amplitude of the first crest and following trough are correctly simulated. For the higher position of the solid, the wave amplitude is underestimated too with an error of about 10 per cent. The trough is better computed at this probe than the first one but there is no clear dispersive tail. We observe the same overall behaviour at probe 4 where most of the initial energy is in the dispersive tail. In both initial configurations, the numerical leading wave propagates a little faster than in the experiment (reaching the gauges 0.1 s before).

Both models correctly reproduce the generation and the propagation of waves generated by subaerial landslides. The SPH method is more accurate to describe the generation of tsunami waves. Nevertheless, it requires a larger computational time than Gerris. However, in spite of the lower accuracy in the initial generation of the wave, Gerris correctly reproduces the overall behaviour during the propagation, using a shorter computational time. Two other validation cases for Gerris dealing with aerial impact and submarine landslide are shown in the appendices.

3 MAXIMUM WAVE ARRIVAL TIME

During the experiments we obtain the arrival time of the leading wave using the different wave gauges. In this section, we develop an analysis within the framework of the shallow water approximation ($kH \ll 1$), and linear waves ($A/H \ll 1$). We consider a subaerial solid landslide where the front basis of the mobile is initially touching the undisturbed free surface. The abscissa origin is located at the intersection of the slope with the horizontal bottom. The abscissa X is measured along the bottom. The solid friction and the mass of the solid are included in the experimentally measured velocity. Fig. 7 illustrates the different parameters used in our study. The validation of the theoretical analysis is studied varying the relevant parameters.

3.1 Scaling laws

For tsunami wave forecast, it is important to predict the arrival time at a fixed point. In the case of earthquake tsunamis, the seafloor deformation occurs instantaneously and does not influence the propagation of waves once generated. On the contrary, for tsunami waves generated by subaerial or submarine landslides, the duration of the collapse in water is a non-negligible parameter. Defining the water depth H, the solid velocity V and the slope angle β, the time of solid sliding t_{solid} is $t_{\text{solid}} = H/(V \sin\beta)$, which is a timescale of the problem. Within the framework of linear non-dispersive waves, the propagation time of the leading wave to reach the probe located at X_p is $t_{\text{travel}} = X_p/\sqrt{gH}$. Consequently, the arrival time of the leading wave at location X_p for a subaerial landslide is given by

$$t_{\max} = \frac{H}{V \sin\beta} + \frac{X_p}{\sqrt{gH}}. \quad (1)$$

The arrival time of the maximum amplitude wave generated by subaerial landslides can be considered as the moving time of the slide down along the slope plus the traveltime of a linear non-dispersive

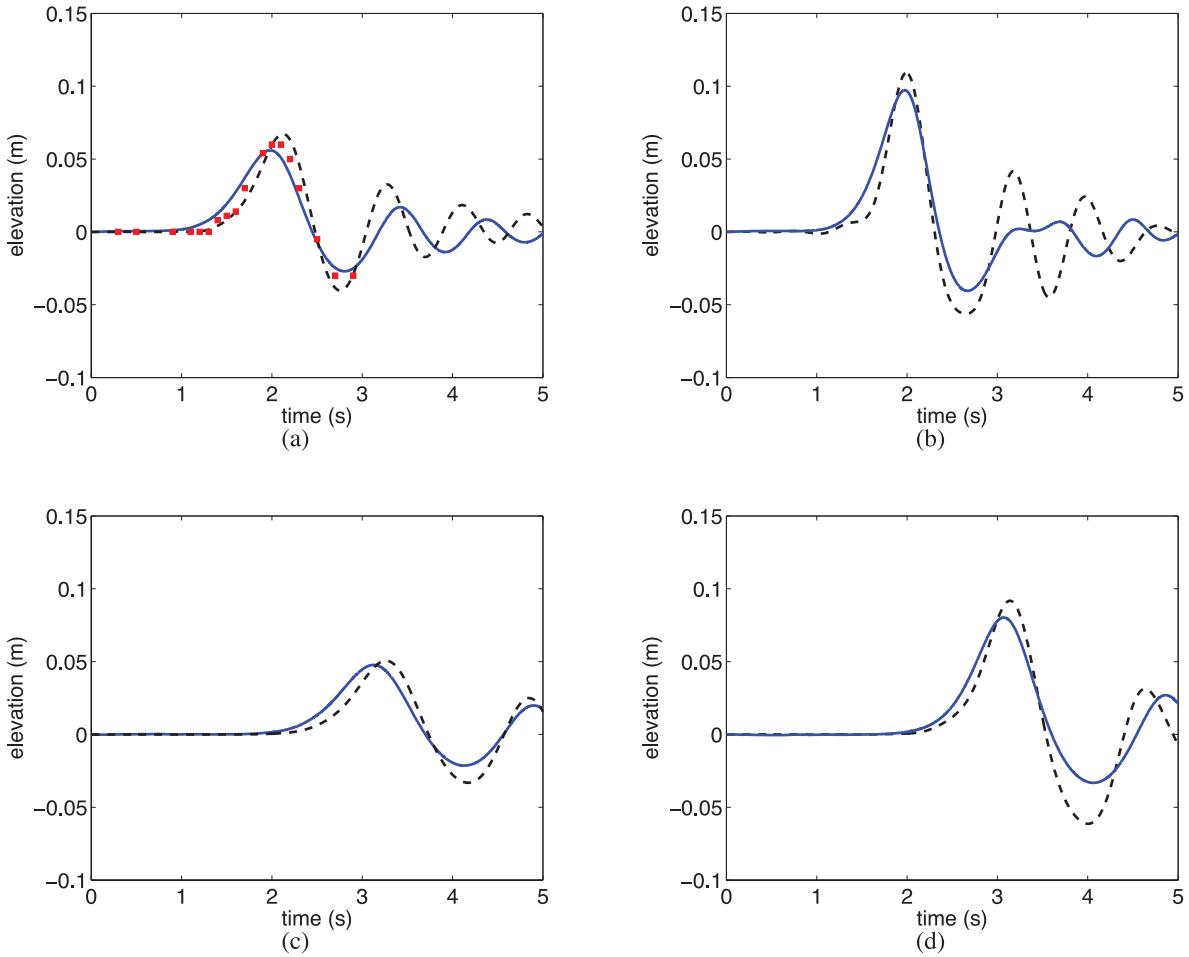

Figure 6. Comparison between experimental and computed wave gauges 2(a,b) and 4(c,d) for both configuration. Experiment (dashed line), Gerris (solid line) and SPH (□). The evolution of the amplitude during the propagation is well represented with Gerris.

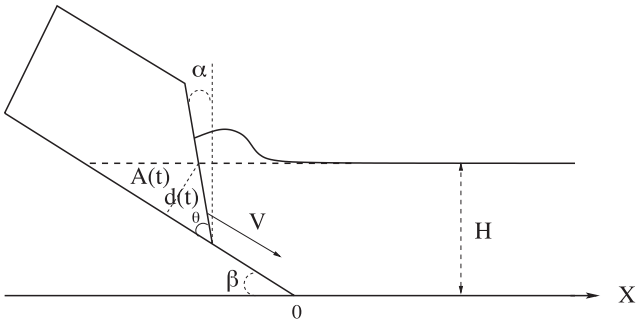

Figure 7. Schematic view of the numerical wave tank at time t. The area of the submerged part of the solid is noted $A(t)$, $d(t)$ is its thickness, β the slope angle, α the angle between the front of the solid and the vertical, H the water depth and V the velocity of the slide.

long wave in water depth H. The error made on the phase velocity by assuming the wave to be non-dispersive is $\mathcal{O}(k^2H^2/6)$ where k is the wavenumber. In all our experiments and numerical simulations, the dispersive parameter satisfies $0.2 < kH < 0.65$ (see Fig. 8a), which leads to an error on the phase velocity of the generated wave varying between 1 and 7 per cent. The generated waves are thus weakly dispersive and the shallow water approximation can be used to estimate the time needed for them to reach the probe located at X_p. In the limit of shallow water waves: $t_{\text{solid}} \ll t_{\text{travel}}$ and $t_{\max} \approx t_{\text{travel}}$; whereas in the limit of large depths, $t_{\text{travel}} \ll t_{\text{solid}}$ and $t_{\max} \approx t_{\text{solid}}$. Thus, we introduce two critical depths $H_{\min}$ and $H_{\max}$. For $H < H_{\min}$, $t_{\max}$ is given by eq. (1) whereas for $H > H_{\max}$, $t_{\max} \approx t_{\text{solid}}$. In this case, the time of generation is large and the wave is not completely formed when the surface deformation arrives at the probe located at X_p. For $H_{\min} < H < H_{\max}$, we approximate $t_{\max}$ by a cubic polynomial: $t_{\max} = \sum_{n=0}^{n=3} a_n H^n$. The depth $H_{\min}$ is chosen so that $\partial_H t_{\max}(H_{\min}) = 0$. The result is

$$H_{\min} = \left[\frac{(X_p\ V\ \sin\beta)^2}{4\,g}\right]^{1/3}. \tag{2}$$

The determination of $H_{\max}$ is more subtle and is defined when $t_{\max}(H_{\max}) = \xi\, t_{\text{solid}}(H_{\max})$, where ξ is a general constant obtained using a unique numerical time-series. From eq. (1) we obtain

$$H_{\max} = \left[\frac{(X_p\ V\ \sin\beta)^2}{(\xi-1)^2\,g}\right]^{1/3}. \tag{3}$$

The two points $[H_{\min}, t_{\max}(H_{\min})]$ and $[H_{\max}, t_{\max}(H_{\max})]$ with their respective tangents of slope 0 and $1/(V\sin\beta)$ allow the computation of the coefficients of the cubic polynomial $a_n(\xi), n = 0, 1, 2, 3$. As previously emphasized, the constant ξ is chosen to give the best agreement with the numerical results ($\xi = 1.2$ for all the probes). The theoretical curve of the function $t_{\max}(H)$ and numerical data at a fixed probe are shown in Fig. 8(b). Note that $H_{\min}$ and $H_{\max}$ depend on the position X_p of the probes.

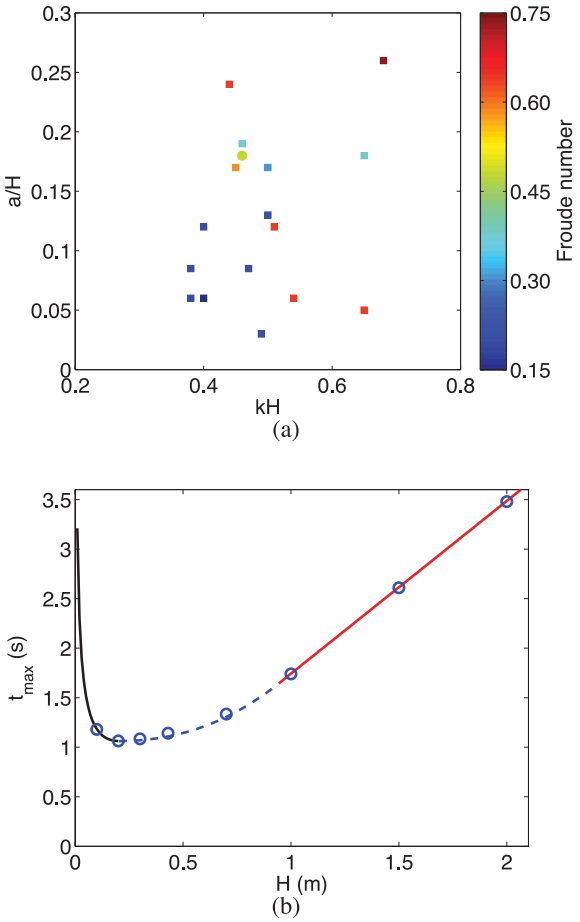

Figure 8. (a) Values of the dispersive and non-linear parameters for several simulations. The Froude number is $V/\sqrt{gH}$. (b) Maximum amplitude arrival time at a fixed probe as a function of depth. Solid black and red lines correspond to the asymptotic behaviours for $H < H_{\min}$ and $H > H_{\max}$, respectively. Dashed blue line corresponds to the approximate solution that matches the asymptotic solutions. Circles correspond to numerical results.

3.2 Comparison between theoretical and numerical results

The numerical simulations are run with the code Gerris, the computed cases correspond to parameters close to the experiments. The theoretical and numerical evolutions of the maximum amplitude arrival time $t_{\max}$ as a function of the different parameters are compared using four probes located respectively at 1, 2, 3 and 6 m from the intersection of the slope with the bottom of the numerical wave tank. $t_{\max}$ is plotted as function of the water depth H in Fig. 9(a) where all the other parameters are set to a constant value. As shown in the previous subsection, $t_{\max}$ admits a minimum value for $H = H_{\min}$. For all the probes, the asymptotic solutions corresponding to $H < H_{\min}$ and $H > H_{\max}$ (solid lines in Fig. 9a) and the matching cubic polynomial (dashed lines in Fig. 9a) agree well with the numerical results. In Fig. 9(b), $t_{\max}$ is plotted as a function of the velocity V of the solid, where all the other parameters are set to a constant value. The theoretical expression (1) of $t_{\max}$ derived in the previous subsection from a dimensional analysis is in very good agreement with the numerical results. We have plotted the value of $t_{\max}$ at the first probe numerically computed with the SPH method for different slide velocities ($V = 0.6$, 1, 2, and 2.5 m). This latter result confirms that our scaling is still consistent for high-speed impact, more accurately simulated with the SPH method. In Figs 10(a) and (b) the behaviour of $t_{\max}$ is shown as a function of the slope angle

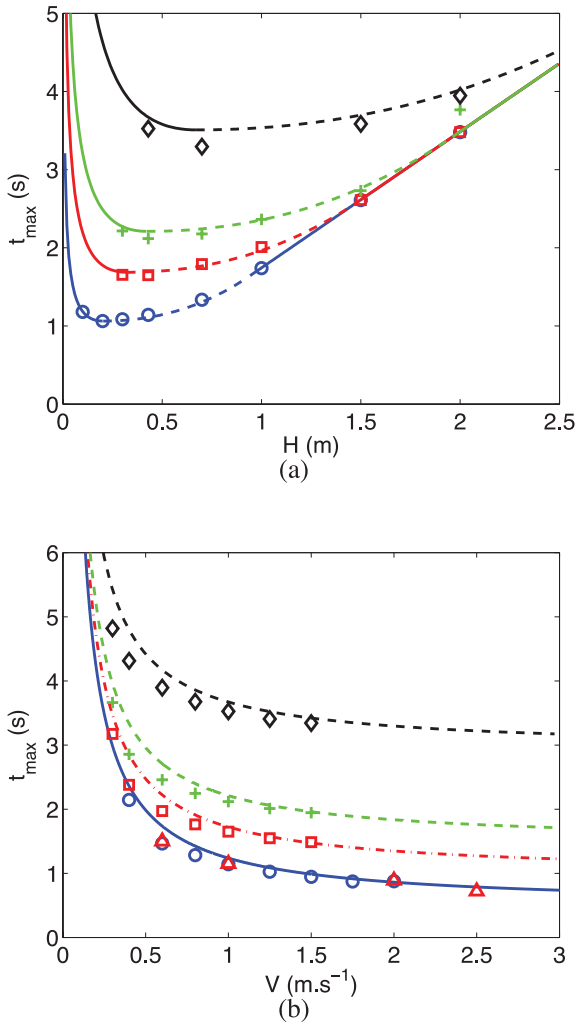

Figure 9. (a) Comparison between numerical and theoretical arrival time of the maximum wave amplitude as a function of the water depth for $\beta = 35°$, $\alpha = 10°$, $V = 1\ \mathrm{m\,s^{-1}}$. The solid lines and dashed lines correspond to the asymptotic solutions and cubic polynomial, respectively. (b) Comparison between numerical and theoretical arrival time of the maximum wave amplitude as a function of the velocity of the slide for $\beta = 35°$, $\alpha = 10°$, $H = 0.43$ m [SPH simulations (△)]. Solid blue, dash-doted red, dashed green and black lines represent the theoretical arrival time at probes 1–4, respectively. Numerical results for probes at: (◯) 1 m, (□) 2 m, (+) 3 m and (◇) 6 m.

β, for two values of the Froude number $Fr = V/\sqrt{gH}$, where all the other parameters are set to a constant value. The agreement between the theoretical results given by eq. (1) and the numerical results is fairly good. For $Fr = 0.2$, we observe a good agreement when the slope is steep or gentle, otherwise some relatively weak discrepancies occur when $20° < \beta < 45°$. For $Fr = 0.64$ and $\beta > 30$, the theory is in better agreement with the numerical simulations. For steep slopes, t_{solid} is short enough to allow a full generation and propagation of the leading wave to the location of the probes. On the contrary, we observed disagreement between theoretical and numerical results for gentle slopes. Note that the ratio of $t_{\mathrm{travel}}/t_{\mathrm{solid}}$ is related to the Froude number defined previously trough the following relation: $t_{\mathrm{travel}}/t_{\mathrm{solid}} = (X_p\, Fr \sin\beta)/H$. For a given Froude number, this ratio decreases as the slope angle decreases (with $0 < \beta < 90°$). The Froude number can also be understood as the ratio between the timescale of wave propagation and the timescale of wave generation.

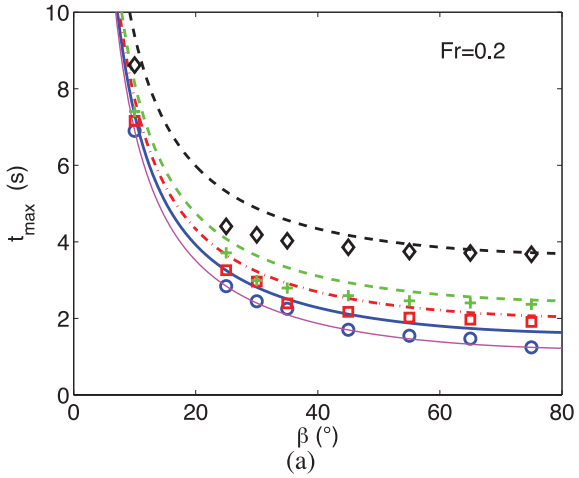

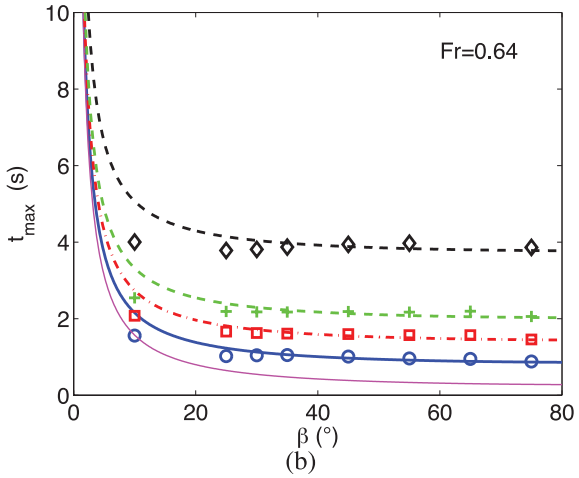

Figure 10. Comparison between numerical and theoretical arrival time of the maximum wave amplitude as a function of the slope angle for (a) $\alpha = 10°$, $V = 0.5\,\mathrm{m\,s^{-1}}$, $H = 0.6\,\mathrm{m}$ and (b) $\alpha = 10°$, $V = 1.1\,\mathrm{m\,s^{-1}}$, $H = 0.3\,\mathrm{m}$. Solid blue, dash-doted red, dashed green and black lines represent the theoretical arrival time at probes 1–4, respectively; The thin magenta solid line corresponds to the case where the gauge is in the generation/transition zone. Numerical results for probes at: (◯) 1 m, (□) 2 m, (+) 3 m and (◇) 6 m.

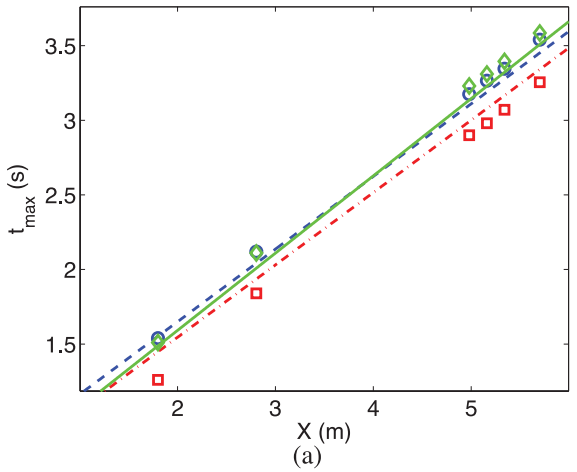

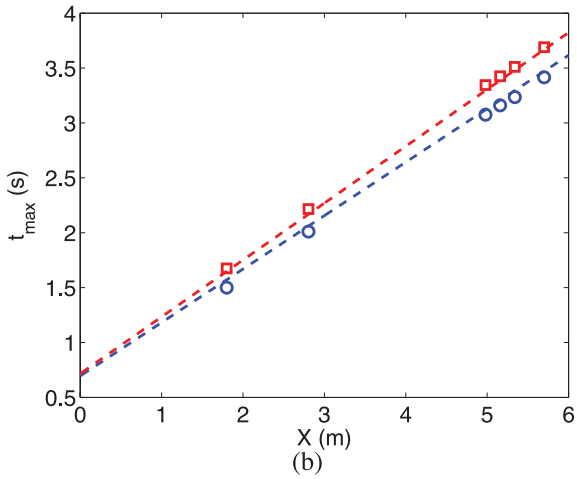

Figure 11. Comparison between experimental and theoretical arrival time of the maximum wave amplitude as a function of the position of probes. (a) Low solid position: (i) for $H = 0.43$ m, $M = 70\,\mathrm{kg}$, $\alpha = 10°$, $\beta = 35°$, dashed line (theory) and blue circles (experiments); (ii) for $H = 0.43$ m, $M = 85.5\,\mathrm{kg}$, $\alpha = 10°$, $\beta = 35°$, dash-dotted line (theory) and red squares (experiments); (iii) for $H = 0.38$ m, $M = 85.5\,\mathrm{kg}$, $\alpha = 10°$, $\beta = 35°$, solid line (theory) and diamonds (experiments). (b) High solid position: (i) for $H = 0.43$ m, $M = 85.5\,\mathrm{kg}$, $\alpha = 10°$, $\beta = 35°$, dashed line (theory) and circles (experiments); (ii) for $H = 0.38$ m, $M = 85.5\,\mathrm{kg}$, $\alpha = 10°$, $\beta = 35°$, dash-dotted line (theory) and squares (experiments).

3.3 Comparison between theoretical and experimental results

To compare the theoretical and experimental arrival time we take into account the mean velocity of the slide along its displacement. This could lead to a little shift in the traveltime of the slide, but it remains less than 0.05 s for all our experiments. This was assumed to have negligeable effects on the laboratory solid landslide. For the low position of the slide one should keep in mind that the traveltime is not $H/(V\sin\beta)$ but $(H - H_s)/(V\sin\beta)$ with H_s the initial submergence of the solid.

In Fig. 11 is shown a comparison between the experimental and theoretical arrival time of the maximum wave amplitude, $t_{\max}$, as a function of the position X_p of the probes. Figs 11(a) and (b) correspond to the low and high positions of the solid, respectively. The theoretical expression (1) is confronted to a series of experiments for different depths and solid masses. Fig. 11(a) shows the effects of both depth and mass on $t_{\max}$ whereas only the influence of the water depth is considered in Fig. 11(b). The leading wave reaches the probes sooner with a heavier solid for a given water depth. Indeed the traveltime of the solid is smaller in this case. It is more difficult to conclude on the effects of the water depth. During our experiments the water depth does not change enough to clearly see its influence, especially on the traveltime of the solid. In all the cases, the experimental and theoretical results are in good agreement.

4 TIME EVOLUTION OF THE MAXIMUM WAVE AMPLITUDE

From the previous section, we are able to predict the arrival time of the leading wave generated by a subaerial solid landslide with a good accuracy. Another property of interest for a tsunami wave, and maybe the most important, is its amplitude. In this section, we derive scaling laws based on a solution of the linearized Korteweg-de-Vries (KdV) equation to predict the evolution of the maximum amplitude as a function of time. The validation and limitations of

these scaling laws are then studied by varying the main parameters of the experiments (V, H, α, β).

4.1 Scaling laws

In the weakly dispersive linear shallow water approximation, the spatio-temporal evolution of the free surface η of an initial perturbation is governed by the linearized KdV equation

$$\frac{\partial \eta}{\partial t} + c\,\frac{\partial \eta}{\partial s} + \frac{c\,h^2}{6}\,\frac{\partial^3 \eta}{\partial s^3} = 0, \tag{4}$$

where h is the local depth and $c = \sqrt{gh}$. For an initial condition $\eta(s, 0) = Q\delta(s)$, the solution of eq. (4) is (see Pelinovsky *et al.* 2000)

$$\eta(s,t) = Q\left(\frac{2}{c\,t\,h^2}\right)^{1/3} \mathrm{Ai}\left[\left(\frac{2}{c\,t\,h^2}\right)^{1/3}(s - c\,t)\right], \tag{5}$$

where Q is a constant corresponding to the cross-section of the water volume moved by the solid, δ the Dirac delta function and Ai the Airy function. This solution corresponds to a leading long wave followed by a modulated wave train. We assume that the solid generates such a perturbation and focus on the leading wave. We use this exact solution derived within the framework of constant depth only to develop a dimensional analysis and we set

$$\eta_{\max} = K_{\mathrm{prop}}\, Q H^{-5/6}\, g^{-1/6}\, t^{-1/3}, \tag{6}$$

where K_{prop} is a dimensionless constant which does not vary with the parameters of the experiments and is going to be determined numerically.

If the solid velocity is larger than the generated wave velocity, the behaviour may be different. Indeed, we may expect the occurrence of two different regimes depending on whether the solid velocity V is larger or smaller than the wave velocity. This leads to define a critical value for the solid velocity. Herein, we use a dimensional analysis based on a simplified theory to determine this critical velocity and the amplitude of the leading front generated by the solid. As soon as the leading front has been generated, it propagates over the slope. Let s be the distance of horizontal propagation of the front, satisfying $s = h/\tan\beta$ where h is the local depth, with $h(t \geq t_{\mathrm{solid}}) = H$. Hence, $0 \leq s(t) \leq H/\tan\beta$. The leading wave velocity along the slope is assumed to be equal to $\sqrt{gh} = \sqrt{g \tan\beta\, s}$. From $c(s) = \mathrm{d}_t s = \sqrt{g \tan\beta\, s}$ the leading wave velocity as a function of time is $c(t) = (g\,t \tan\beta)/2$. The temporal mean velocity of the front during its propagation over the slope is

$$\bar{c} = \frac{1}{t_b}\int_0^{t_b} c\,\mathrm{d}t = \frac{\sqrt{gH}}{2}, \tag{7}$$

where t_b satisfies $s(t_b) = H/\tan\beta$. Using $\bar{c}$ as the critical solid velocity, the critical corresponding Froude number is $Fr = 1/2$. In the numerical simulations presented in Section 3, we found two different regimes depending on whether the Froude number is larger or smaller than the value 1/2. For large solid velocity $V > \bar{c}$ or $Fr > 1/2$, we assume that $Q = A_0$, where $A_0 = A(t = t_{\mathrm{solid}})$ is the submerged part of the solid as defined in Fig. 7 at time $t = t_{\mathrm{solid}}$. For slower solid velocity ($Fr < 1/2$), we consider the thickness of the submerged part of the solid, $d_0 = [H\cos(\alpha + \beta)]/\cos\alpha$, as defined in Fig. 7 at time $t = t_{\mathrm{solid}}$. The thickness parameter has been used in several studies on landslide tsunami forecast (Fritz 2002; Walder *et al.* 2003; Fritz *et al.* 2004). Thus, the coefficient Q is defined as follows:

$$Q \sim \begin{cases} A_0 & \text{if} \quad Fr > \frac{1}{2}, \\ a\,H\,\frac{\cos(\alpha+\beta)}{\cos\alpha} & \text{if} \quad Fr < \frac{1}{2}, \end{cases} \tag{8}$$

where a a is a characteristic lengthscale of the problem, related to the generated wave. To define a, we assume that all the energy of the solid landslide is transferred in the linear generated wave, which leads to : $\rho g a^2 = \rho V^2 L$, where L is a typical length of the solid defined as the square root of its submerged part area A_0 (see Fig. 7) and a the amplitude of the linear wave. Based on this, we derive $a = V\,A_0^{1/4} g^{-1/2}$.

Combining eqs (6) and (8) we get for the elevation of the leading wave

$$\eta_{\max} = \begin{cases} K_{\mathrm{prop1}}\, A_0\, H^{-5/6}\, g^{-1/6}\, t^{-1/3}, \\ K_{\mathrm{prop2}}\, \zeta\, A_0^{1/4}\, V\, H^{1/6}\, g^{-2/3}\, t^{-1/3}. \end{cases} \tag{9}$$

The first equation with K_{prop1} is for $Fr > 1/2$, the second one with K_{prop2} is for $Fr < 1/2$ with $\zeta = [\cos(\alpha + \beta)/\cos\alpha]$. The submerged area of the solid A_0 is

$$A_0 = \frac{H^2 \cos(\alpha + \beta)}{2 \sin\beta\, \cos\alpha}. \tag{10}$$

These previous expressions provide the temporal evolution of the maximum amplitude of the generated leading wave in the propagation regime which can be considered as the regime in the far field. In the generation stage, the free-surface elevation increases during the displacement of the solid and reaches its maximum at $t = t_{\mathrm{solid}}$. Contrary to the propagation regime, we do not have an analytical expression of the wave profile during the phase of the wave generation by the solid landslide. Hence, the derivation of the analytical expression of the amplitude of the generated wave is based on a dimensional analysis relied on numerical results. From the numerical simulations we observed that the amplitude increases as $\sqrt{t}$ during the solid motion (see Fig. 12). To hold $Fr = 1/2$ as critical Froude number, the maximum elevation is sought in the form

$$\eta_{\max} = K_{\mathrm{gen}}\, Q^{\gamma}\, V^{\lambda}\, t^{1/2}, \tag{11}$$

where K_{gen} is a dimensionless constant. A dimensional analysis gives $\gamma = 1/4$ and $\lambda = 1/2$. Hence, in the generation regime

$$\eta_{\max} = \begin{cases} K_{\mathrm{gen1}}\, A_0^{1/4}\, V^{1/2}\, t^{1/2}, \\ K_{\mathrm{gen2}}\, \zeta^{1/4}\, A_0^{1/16}\, V^{3/4}\, H^{1/4} g^{-1/8}\, t^{1/2}. \end{cases} \tag{12}$$

The first equation with K_{gen1} is for $Fr > 1/2$, the second one with K_{gen2} is for $Fr < 1/2$.

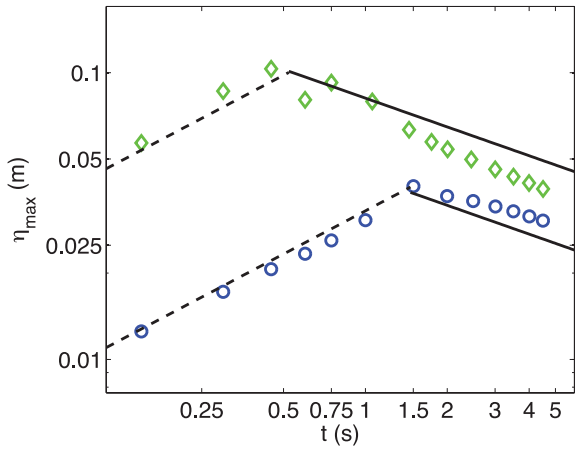

Figure 12. Temporal evolution of the leading wave amplitude for two initial sets of parameters (logarithmic scales). $V = 0.5$ m s^{-1}, $H = 0.6$ m, $\beta = 55°$ and $\alpha = 10°$ (◯). $V = 1$ m s^{-1}, $H = 0.3$ m, $\beta = 35°$ and $\alpha = 10°$ (◇). Slope 1/2 (dashed lines) and slope $-1/3$ (solid lines).

4.2 Validation and limitation of the derived scaling laws

Under different assumptions, scaling laws depending on the Froude number, and based on a dimensional analysis have been derived. Two different regimes are defined as a function of the sliding duration of the solid and the distance from the shore. A generation regime corresponding to the evolution of the amplitude in the near-field and a propagation regime, where the generated waves behave linearly in shallow water approximation. Herein, the validity of the approximate solution is checked for $Fr < 1/2$ and $Fr > 1/2$, varying the main parameters of the problem V, H, β and α (see Table 2).

Several numerical simulations have been run by varying only the slide velocity V from 0.3 to 2.5 m s^{-1}. The other parameters are $H = 0.43$ m, $\beta = 35^\circ$ and $\alpha = 10^\circ$. The numerical wave gauges are located at the same position as previously. For all the simulations, they are located in the propagation zone (the maximum amplitude at the probes occurring after the end of the solid displacement). The maximum amplitude as a function of the solid velocity is shown in Fig. 13. The black vertical line corresponds to $Fr = 1/2$ and separates the domains corresponding to $Fr < 1/2$ and $Fr > 1/2$, respectively. From both sides of the critical line the theoretical results are in good agreement with those of the numerical simulations. The main discrepancy occurs in the vicinity of $Fr = 1/2$ because we did not use a matching of the solutions. The elevation at the first probe is computed using the SPH method that provides amplitudes larger than those of Gerris (which is consistent with previous observations). However, the overall behaviour from both methods is the same. The values of K_{prop1} and K_{prop2} are defined so as to match Gerris results. These coefficients remain almost unchanged when one considers SPH simulations. The values of the coefficients are $K_{\text{prop1}} = 0.78$ and $K_{\text{prop2}} = 1.8$.

The influence of the velocity having been studied, we proceed in a similar way to quantify the influence of the water depth. Several numerical simulations are now run by varying only the water depth from $H = 0.2$ m to $H = 2$ m. All the other parameters are fixed: $V = 1$ m s^{-1}, $\beta = 35^\circ$ and $\alpha = 10^\circ$. As previously, the critical vertical black line corresponds to $Fr = 1/2$. The maximum amplitude in the propagation zone as a function of H can be seen in the Fig. 14(a). Theoretical and numerical results are in good agreement (as also shown by the first wave gauge results of two SPH complementary simulations). Here again, SPH results are slightly higher than those of Gerris, but the trend remains consistent with the theory. In the generation stage (Fig. 14b)

Table 2. Notations and parameters values used for numerical simulations.

Parameter	Notation	Range of parameters
Solid velocity	V	0.3–2.5 m s^{-1}
Water depth	H	0.2–2 m
Slope angle	β	5–75°
Solid angle	α	0–52°

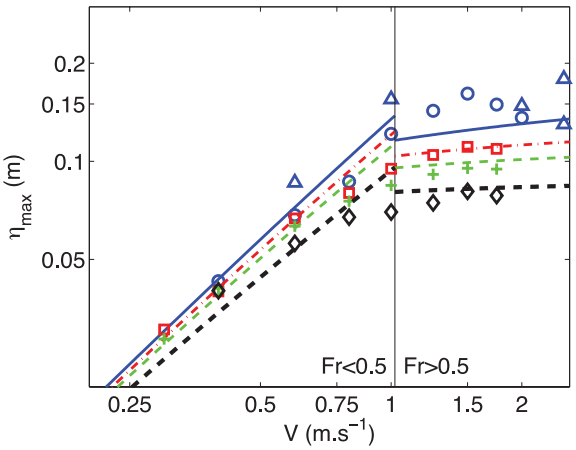

Figure 13. Numerical and theoretical maximum amplitude as a function of the slide velocity (logarithmic scales). Markers correspond to numerical wave probes: First probe (◯) for Gerris and (△) for SPH, second probe (□), third probe (+) and fourth probe (◇). Curves correspond to theoretical results: First probe (solid line), second probe (dot-dashed line), third probe (thin dashed line) and fourth probe (thick dashed line). Theory is in a satisfactory agreement with the simulations even for a Froude number close to 1/2.

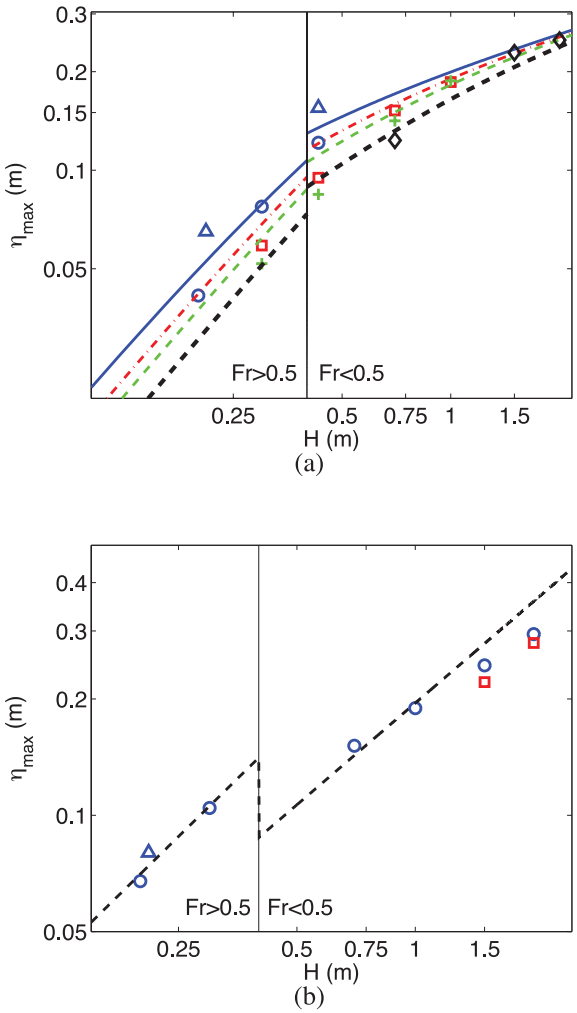

Figure 14. Numerical and theoretical maximum amplitude as a function of depth: (a) in propagation regime and (b) in generation regime. Markers correspond to numerical wave probes and curves to theoretical results (logarithmic scales). (a) First probe (◯) for Gerris and (△) for SPH, second probe (□), third probe (+) and fourth probe (◇). First probe (solid line), second probe (dot-dashed line), third probe (thin dashed line) and fourth probe (thick dashed line). (b) First probe (◯ for Gerris and △ for SPH), second probe (□). Theory is in good agreement with the simulations.

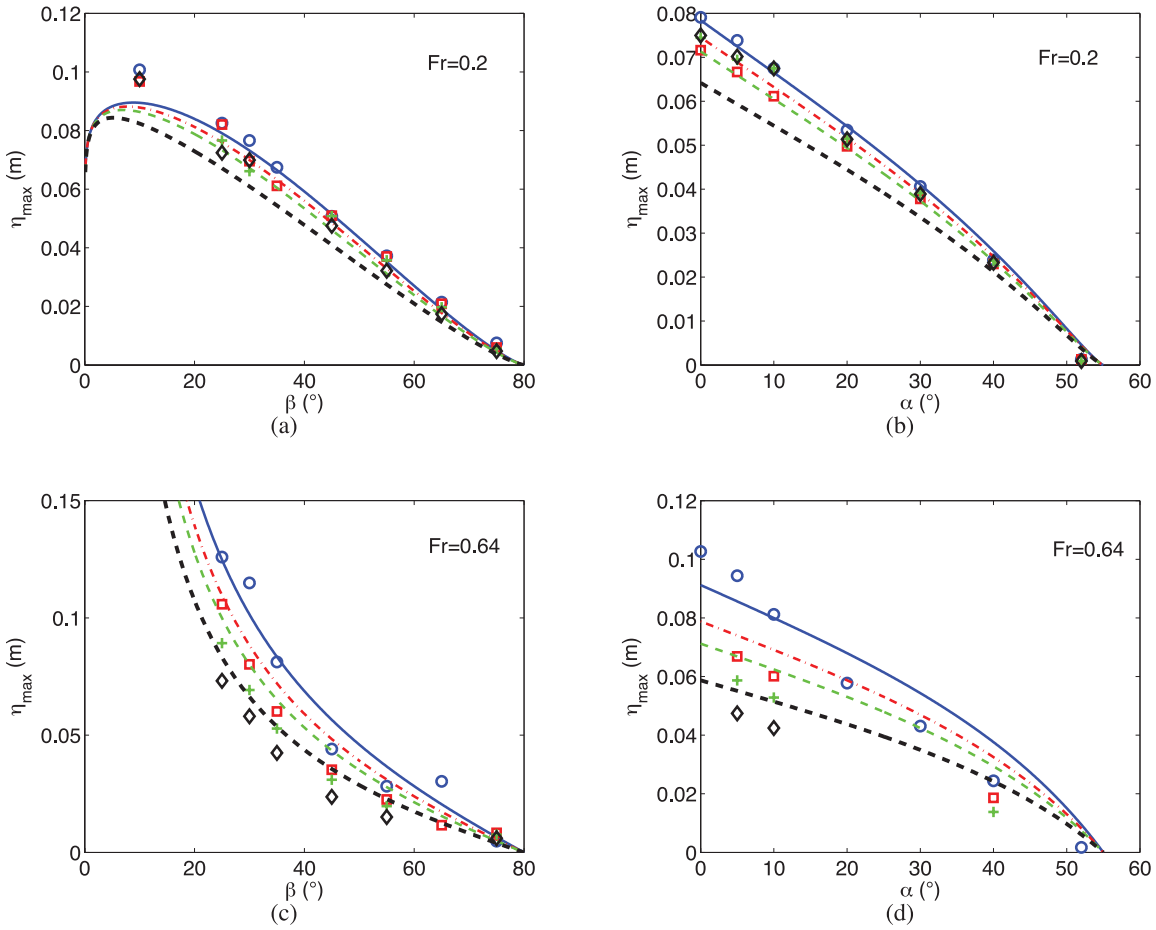

Figure 15. Numerical and theoretical maximum amplitude as a function of the slope angle [panels (a) and (c)] and angle α [panels (b) and (d)]. Markers correspond to numerical wave probes and curves to theoretical results. First probe (◯), second probe (□), third probe (+) and fourth probe (◇). First probe (solid line), second probe (dot-dashed line), third probe (thin dashed line) and fourth probe (thick dashed line).

when $Fr > 1/2$, the theory is in excellent agreement with the numerical simulations ($K_{\text{gen1}} = 0.30$). For $Fr < 1/2$, the theory is also in good agreement with the numerical results using $K_{\text{gen2}} = 0.22$.

In addition to the slide velocity and the water depth, we also check the validity of the approximate solution with the slide geometry. Numerical simulations are performed by varying the slope angle and the angle between the front of the solid and the vertical for two values of the Froude number larger and smaller than 1/2, respectively. In Fig. 15(a) is plotted the maximum amplitude recorded at different numerical wave probes for several values of β and $Fr = 0.2$ ($V = 0.5\ \text{m s}^{-1}$, $H = 0.6$ m and $\alpha = 10°$). The corresponding theoretical curves given by eq. (9) are very close to the numerical points. Nevertheless, a discrepancy can be observed between numerical and theoretical results for small β. Note that our theory becomes invalid for β close to zero. Fig. 15(b) illustrates the influence of α for $V = 0.5\ \text{m s}^{-1}$, $H = 0.6$ m and $\beta = 35°$. Here again the theory is consistent with the numerical simulations. The same comparisons are presented in Figs 15(c) and (d) for $Fr = 0.64$. The agreement between theoretical and numerical results is good again. The previous comparisons between theoretical results and numerical simulations have demonstrated the validity of eqs (9) and (12) to provide a good estimate of the amplitude of the leading water wave.

Results derived in Sections 3 and 4 are summarized in Fig. 16 where the time evolution of the amplitude of the leading wave for two cases corresponding to $Fr < 1/2$ and $Fr > 1/2$, respectively, is shown. The solid lines correspond to eq. (9) and describe the propagation regime ($t > t_{\text{solid}}$): the leading wave amplitude decreases as $t^{-1/3}$. The dashed lines correspond to eq. (12) associated with the

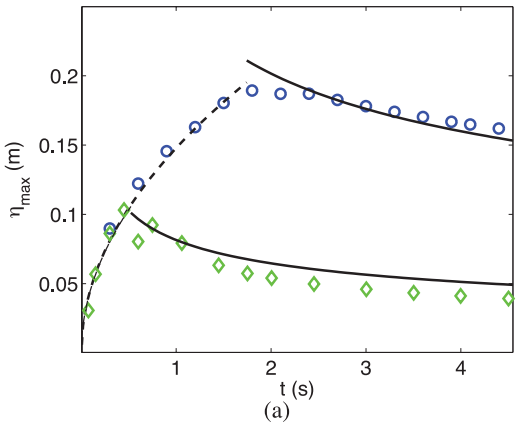

Figure 16. Numerical and theoretical temporal evolutions of leading wave amplitude for two cases corresponding to $V = 1\ \text{m s}^{-1}$, $H = 1$ m, $\beta = 35°$, $\alpha = 10°$ (circles and $Fr < 1/2$) and $V = 1\ \text{m s}^{-1}$, $H = 0.3$ m, $\beta = 35°$, $\alpha = 10°$ (diamonds and $Fr > 1/2$), respectively. Solid and dashed lines correspond to eqs (9) and (12), respectively. An excellent agreement between the theory and numerical simulations is obtained.

generation regime ($t < t_{solid}$): the leading wave amplitude increases as $t^{1/2}$. The agreement between theoretical and numerical results is good except around $t = t_{solid}$ which separates the two regimes.

5 APPLICATION OF THE DERIVED SCALING LAWS

In the previous section we have obtained scaling laws to predict the time evolution of the maximum amplitude of a wave generated by a solid landslide. To confirm their forecast abilities, we compare them with two laboratory experiments.

5.1 Comparison with our experiments

To compare the previously obtained results and experimental ones under similar conditions, we have to define the velocity of the solid. Indeed, in the experiment this velocity is not constant anymore but is time dependent. The first approximation is to consider the mean velocity of the mobile during its motion. We may expect that the corresponding dimensional analysis solution will underestimate the amplitude of the generated wave. Another possibility is to consider the maximum velocity of the slide. In this case we can expect an overestimate of the amplitude of the generated wave. Fig. 17 shows a comparison between experimental, numerical and dimensional analysis amplitude evolution as a function of time for two subaerial experiments corresponding to $H = 0.43$ m and $H = 0.38$ m, respectively. For both experiments, the slope angle is $\beta = 35^\circ$, the angle between the front of the solid and the vertical is $\alpha = 10^\circ$ and the mass is the same. In the generation regime, the dashed lines correspond to a slide with a constant velocity $V = V_{max}$ (with $V_{max} = 1.56\ \mathrm{m\,s^{-1}}$)and $Fr > 1/2$ whereas the dot-dashed lines correspond to $V = V_{mean}$ (with $V_{mean} = 0,99\ \mathrm{m\,s^{-1}}$) and $Fr < 1/2$. Wave propagation begins as soon as the solid reaches the bottom of the tank. In this regime, we use the mean velocity of the slide to compute the Froude number and select the appropriate formula. In both experiments, the Froude number in the propagation regime remains smaller than $1/2$. In Fig. 17(a), experimental and numerical results are in relative good agreement. The results given by SPH and Gerris are quite similar. As expected, the scaling law (12) for $Fr < 1/2$ underestimates the leading wave amplitude but the one for $Fr > 1/2$ (taking into account the maximum velocity of the solid) is in a good agreement with the numerical simulations. Nevertheless the theory correctly describes the behaviour of the amplitude. Once the solid reaches the bottom of the tank, the generation stage ends and the wave amplitude decreases as $t^{-1/3}$ during the propagation regime. The small difference between theoretical and experimental results is due to the fact that the considered Froude number is very close to the critical value $Fr = 1/2$. For the lower water depth (Fig. 17b), the numerical, experimental and dimensional analysis' results are in an excellent agreement.

5.2 Comparison with Heinrich's experiments

We have compared our theoretical results with the subaerial experimental data of Heinrich (1992) presented above in subsection B. The initial water depth is $H = 0.4$ m, the slope angle $\beta = 45^\circ$ and the solid impacts the undisturbed free surface vertically which corresponds to $\alpha = 0^\circ$. The vertical displacement of the solid during the experiment was given in Heinrich (1992), allowing the computation of the solid velocity. Fig. 18 displays the experimental, numerical

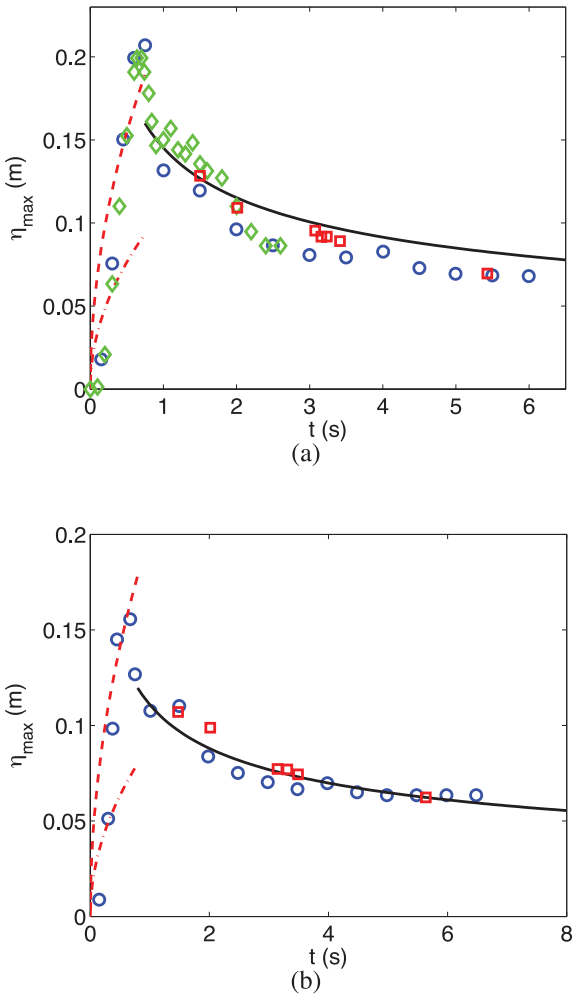

Figure 17. Temporal evolution of the leading wave amplitude for (a) $H = 0.43$ m and (b) $H = 0.38$ m. Experiments (□), Gerris simulation (◯), SPH simulation (◇), dimensional analysis in the propagation stage (solid lines), in the generation stage (dashed lines for $V = V_{max}$ and dot-dashed lines for $V = V_{mean}$).

and theoretical time evolution of the maximum amplitude for the subaerial experiment conducted by Heinrich (1992). As previously, in the generation zone, we consider two cases: $V = V_{mean}$ and $V = V_{max}$. The mean velocity of the solid is about $0.97\ \mathrm{m\,s^{-1}}$, corresponding to $Fr = 0.49$. During the propagation, both scalings for $Fr < 1/2$ and $Fr > 1/2$ are used (eq. 9). One can observe in the propagation regime that the dimensional analysis overestimates the experimental results for $Fr < 1/2$ whereas Gerris underestimates them. As discussed previously, the weak discrepancy observed between theoretical and experimental results may be explained by the fact that the Froude number is very close to the critical value $Fr = 1/2$.

6 CONCLUSION

An experimental, numerical and analytical investigation on waves generated by solid subaerial landslides is reported. Numerical simulations are run with two different codes based on the smoothed-particle hydrodynamics (SPH) method and on the Finite-volume method, respectively. We have shown that both methods are quite

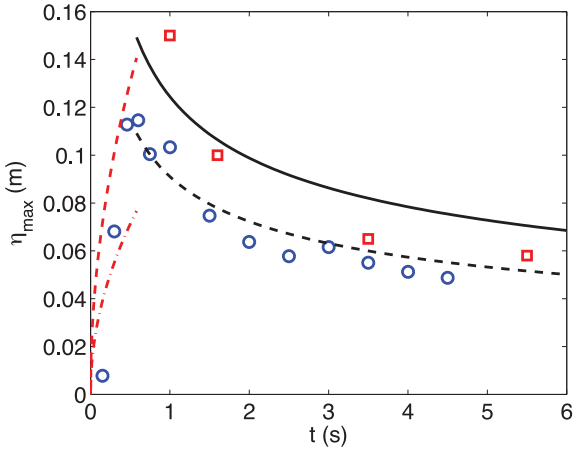

Figure 18. Temporal evolution of the leading wave amplitude in the case of Heinrich's experiments: comparison between experimental results (□), Gerris results (◯) and our proposed scaling laws in the propagation regime (solid line for $Fr < 1/2$ and black dashed line for $Fr > 1/2$), in the generation regime (red dashed line for $V = V_{max}$ and dot-dashed line for $V = V_{mean}$).

complementary, SPH being more accurate in the generation stage but very expensive for the simulation of the propagation, whereas Gerris can efficiently simulate the propagation. Furthermore, based on the numerical simulations, scaling laws on the temporal evolution of the leading wave amplitude are derived for the generation and propagation regimes, respectively. From these laws, we can claim that for waves generated by solid landslides the most important parameters are the velocity of the slide and water depth. Indeed, generation and propagation both depend on the Froude number which is directly linked to those parameters. This is consistent with previous studies (Kamphuis & Bowering 1972; Walder *et al.* 2003). The validity of these approximate solutions derived from a dimensional analysis is tested by comparison with present experiments and those of Heinrich (1992). The comparison demonstrates that the results obtained from theoretical approximations and numerical models are in good agreement with the experimental data.

However, an improvement of the theory is needed to describe more realistic cases of tsunami waves generated by subaerial landslides, namely in the generation stage. Indeed, waves generated by subaerial landslides depend strongly on the slide parameters, namely the volume, velocity and rigidity of the slide (Fritz 2002; Ataie-Ashtiani & Nik-Khah 2008). Experiments and numerical simulations are in progress with granular media to study the influence of the slide rheology on the generated waves. A similar study is currently underway to extend our results to cases where 3-D effects are important.

ACKNOWLEDGEMENTS

For this work, D. Cébron was partially supported by the ETH Zürich Postdoctoral fellowship Progam as well as by the Marie Curie Actions for People COFUND Program.

REFERENCES

Abadie, S., Morichon, D., Grilli, S. & Glockner, S., 2010. Numerical simulation of waves generated by landslides using a multiple-fluid Navier-Stokes model, *Coast. Eng.,* **57**(9), 779–794.

Abadie, S., Harris, J., Grilli, S. & Fabre, R., 2012. Numerical modeling of tsunami waves generated by the flank collapse of the Cumbre Vieja Volcano (La Palma, Canary Islands): tsunami source and near field effects, *J. geophys. Res.,* **117,** C05030, doi:10.1029/2011JC007646.

Assier-Rzadkieaicz, S., Heinrich, P., Sabatier, P., Savoye, B. & Bourillet, J., 2000. Numerical modelling of a landslide-generated tsunami: the 1979 Nice event, *Pure appl. Geophys.,* **157**(10), 1707–1727.

Ataie-Ashtiani, B. & Nik-Khah, A., 2008. Impulsive waves caused by subaerial landslides, *Environ. Fluid Mech.,* **8**(3), 263–280.

Cébron, D. & Sigrist, J., 2008. Toward a 2D SPH multiphysic code with solid-solid & fluid interactions for industrial related problems, in *Proceedings of the 8th International Conference on Hydrodynamics,* Nantes, France.

Dalrymple, R. & Rogers, B., 2006. Numerical modeling of water waves with the SPH method, *Coast. Eng.,* **53**(2–3), 141–147.

Didenkulova, I., Nikolkina, I., Pelinovsky, E. & Zahibo, N., 2010. Tsunami waves generated by submarine landslides of variable volume: analytical solutions for a basin of variable depth, *Nat. Hazard Earth Syst. Sci.,* **10,** 2407–2419.

Enet, F. & Grilli, S. *et al.*, 2007. Experimental study of tsunami generation by three-dimensional rigid underwater landslides, *J. Waterway, Port, Coast. Ocean Eng.,* **133,** 442–454.

Fernandez-Nieto, E.D., Bouchut, F., Brech, D., Castro-Diaz, M.J. & Mangeney, A., 2008. A new Savage-Hutter type model for submarine avalanches and generated tsunami, *J. Comput. Phys.,* **227**(16), 7720–7754.

Fritz, H.M., 2002. Initial phase of landslide generated impulse waves, *PhD thesis,* Nr. 14871, Swiss Federal Institute of Technology (ETH), Zürich.

Fritz, H.M., Hager, W.H. & Minor, H.-E., 2003a. Landlside generated impulse waves; part 1: instantaneous flow fields, *Exp. Fluids,* **35,** 505–519.

Fritz, H.M., Hager, W.H. & Minor, H.-E., 2003b. Landlside generated impulse waves; part 2: hydrodynamic impact craters, *Exp. Fluids,* **35,** 520–532.

Fritz, H., Hager, W. & Minor, H., 2004. Near field characteristics of landslide generated impulse waves, *J. Waterway, Port, Coast. Ocean Eng.,* **130,** 287–302.

Fritz, H.M., Mohammed, F. & Yoo, J., 2009. Lituya Bay landslide impact generated mega-tsunami 50th anniversary, *Pure appl. Geophys.,* **166**(1–2), 153–175.

Glicken, H., Meyer, W. & Sabol, M., 1989. Geology and Ground-Water Hydrology of Spirit Lake Blockage, Mount St. Helens, Washington, with Implications for Lake Retention *U.S. Geophys. Surv. Bull.,* **1789,** 33.

Gómez-Gesteira, M., Rogers, B., Dalrymple, R., Crespo, A. & Narayanaswamy, M., 2010. User Guide for the SPHysics Code v2.0, http://www.sphysics.org.

Gómez-Gesteira, M., Rogers, B.D., Crespo, A.J.C., Dalrymple, R., Narayanaswamy, M. & Dominguez, J.M., 2012a. SPHysics—development of a free-surface fluid solver—Part 1: theory and Formaulation, *Comput. Geosci.,* **48,** 289–299.

Gómez-Gesteira, M., Crespo, A.J.C., Rogers, B.D., Dalrymple, R., Dominguez, J.M. & Barreiro, A., 2012b. SPHysics—development of a free-surface fluid solver—Part 2: efficiency and test cases, *Comput. Geosci.,* **48,** 300–307.

Grilli, S., Vogelmann, T. & Watts, P., 2002. Development of a 3D Numerical Wave Tank for modeling tsunami generation by underwater landslides, *Eng. Anal. Bound. Elem.,* **26**(4), 301–313.

Grilli, S., Ioualalen, M., Asavanant, J., Shi, F., Kirby, J. & Watts, P., 2007. Source constraints and model simulation of the December 26, 2004, Indian Ocean tsunami, *J. Waterway, Port, Coast. Ocean Eng.,* **133,** 414–428.

Heinrich, P., 1992. Nonlinear water waves generated by submarine and aerial landslides, *J. Waterway, Port, Coast. Ocean Eng.,* **118,** 249–266.

Heinrich, P., Piatanesi, A. & Hebert, H., 2001. Numerical modelling of tsunami generation and propagation from submarine slumps: the 1998 Papua New Guinea event, *Geophys. J. Int.,* **145**(1), 97–111.

Kamphuis, J. & Bowering, R., 1972. Impulse waves generated by landslides, in *Proceedings of 12th ICCE,* Vancouver, Canada. ASCE, pp. 575–588.

Kharif, C. & Pelinovsky, E., 2005. Asteroid impact tsunamis, *Comptes Rendus Phys.,* **6**(3), 361–366.
Law, L. & Brebner, A., 1968. On water waves generated by landslides, in *Proceedings of the Third Australasian Conference on Hydraulics and Fluid Mechanics,* Sydney, Australia, pp. 155–159.
Levin, B. & Nosov, M., 2009. Physics of Tsunamis, Vol. XI, Springer, 327p.
Liu, P., Wu, T., Raichlen, F., Synolakis, C. & Borrero, J., 2005. Runup and rundown generated by three-dimensional sliding masses, *J. Fluid Mech.,* **536**(1), 107–144.
Lo, E. YM. & Shao, S., 2002. Simulation of near-shore solitary wave mechanics by an incompressible SPH method, *Appl. Ocean Res.,* **24**(5), 275–286.
Lovholt, F., Pedersen, G. & Gisler, G., 2008. Oceanic propagation of a potential tsunami from the La Palma Island, *J. geophys. Res.,* **113,** C09026, doi:10.1029/2007JC004603.
McMurtry, G., Fryer, G., Tappin, D., Wilkinson, I., Williams, M., Fietzke, J., Garbe-Schoenberg, D. & Watts, P., 2004. Megatsunami deposits on Kohala volcano, Hawaii, from flank collapse of Mauna Loa, *Geology,* **32**(9), 741–744.
Mohammed, F. & Fritz, H.M., 2012. Physical modeling of tsunamis generated by three-dimensional deformable granular landslides, *J. geophys. Res.,* **117,** C11, doi:10.1029/2011JC007850.
Monaghan, J., 1989. On the problem of penetration in particle methods, *J. Comput. Phys.,* **82**(1), 1–15.
Monaghan, J., 1992. Smoothed particle hydrodynamics, *Annu. Rev. Astron. Astrophys.,* **30,** 543–574.
Monaghan, J. & Kos, A., 2000. Scott Russell's wave generator, *Phys. Fluids,* **12,** 622–630.
Murty, T., 1979. Submarine slide-generated water waves in Kitimat Inlet, *British Columbia, J. Geophys. Res,* **84,** 7777–7779.
Pelinovsky, E. & Poplavsky, A., 1996. Simplified model of tsunami generation by submarine landslides, *Phys. Chem. Earth,* **21**(1–2), 13–17.
Pelinovsky, E., Talipova, T. & Kharif, C., 2000. Nonlinear-dispersive mechanism of the freak wave formation in shallow water, *Physica D: Nonlinear Phenom.,* **147**(1–2), 83–94.
Popinet, S., 2003. Gerris: a tree-based adaptive solver for the incompressible euler equations in complex geometries, *J. Comput. Phys.,* **190**(2), 572–600.
Popinet, S., 2009. An accurate adaptive solver for surface-tension-driven interfacial flows, *J. Comput. Phys.,* **228**(16), 5838–5866.
Rogers, B. & Dalrymple, R., 2008. SPH modeling of tsunami waves, *Adv. Numer. Models Simul. Tsunami Waves Runup,* **10,** 75–100.
Sammarco, P. & Renzi, E., 2008. Landslide tsunamis propagating along a plane beach, *J. Fluid Mech.,* **598,** 107–119.
Walder, J., Watts, P., Sorensen, O. & Janssen, K., 2003. Tsunamis generated by subaerial mass flows, *J. geophys. Res,* **108**(85), 1–19.
Ward, S. & Day, S., 2001. Cumbre Vieja Volcano—potential collapse and tsunami at La Palma, Canary Islands, *Geophys. Res. Lett,* **28**(17), 3397–3400.
Watts, P., 1997. Water waves generated by underwater landslides, *PhD thesis,* California Institute of Technology.

APPENDIX A: SCOTT RUSSELL'S WAVE GENERATOR

After some experiments on design for canal boat, the naval engineer John Scott Russell discovered the solitary wave. He explained that the mass of water accumulated round the prow of the vessel leave it behind when it suddenly stops. He experimentally reproduced a solitary wave in a long rectangular tank with a weighted box falling down vertically in water. To validate the numerical model, we compare our simulation results to the experiments of Monaghan & Kos (2000).

Monaghan and Kos' experiments have been conducted in a 9-m-long, 0.4-m-high and 0.4-m-wide wave tank. The box has a length of 0.3 m, a width of 0.39 m, a height of 0.4 m and a weight of 38.2 kg. Three experiments were done at different water depths ($D = 0.116$, 0.21 and 0.288 m), the initial position of the box was 0.5 cm above the undisturbed free surface and 2 cm from the left side of the tank. Time evolution of the free surface deformations is measured with a wave gauge located at 1.2 m from the left side of the canal. From those experiments they observed that in the three cases the main behaviour was the same. A vortex occurred at the lower right corner of the box and was advected rightward. One can also note the increase of the amplitude of the solitary wave when the water depth decreases. A numerical simulation was performed for each water depth. In our model, the free fall is not implemented: the velocity of the solid is imposed all along the motion. We consider the experimental data given in Monaghan & Kos (2000) for the three cases. In Fig. A1 comparisons between snaphots of the experiment and numerical results are shown for a water depth $D = 0.21$ m. As in the experiment, a vortex can be observed in the lower right corner of the block and is advected rightward during the motion. At $t = 0.27$ s, we observe the formation

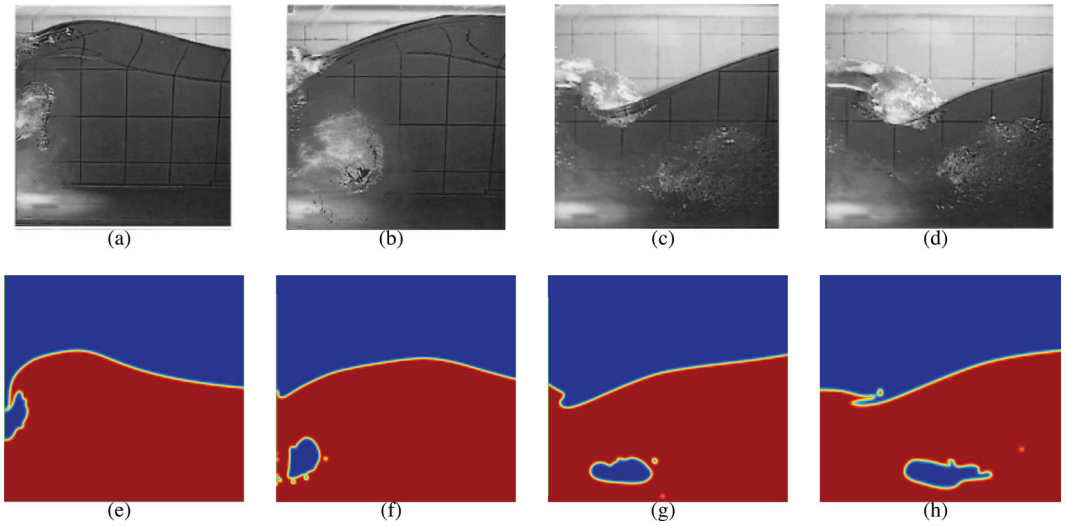

Figure A1. Comparison between Monaghan & Kos' experiments and present numerical simulations for a depth $D = 0.21$ m. Time increases from left to right: $t = 0.21$, 0.42, 0.61 and 0.70 s.

Table A1. Wave amplitude in metres for the experiments and simulations with different levels of refinement. As expected, increasing the refinement improves the accuracy of the results. Numerical errors at level 7 is shown in Fig. A2(b).

	Experiments	Level 6	Level 7	Level 8
$D = 0.116$ m	0.109 ± 0.02	0.084	0.096	0.092
$D = 0.21$ m	0.092 ± 0.01	0.106	0.097	0.093
$D = 0.288$ m	0.093 ± 0.01	0.133	0.099	0.095

of a reverse plunging wave impacting the solid. This has also been observed by Monaghan & Kos (2000) in their experiments and simulations. Our numerical simulations qualitatively agree with their experiments.

Table A1 shows the wave amplitude for the experiments and simulations, respectively. Results are given for three different spatial resolution in the three considered cases in the experiments. Here again we use the values of density and viscosity for air and water at ambient temperature, the solver is tuned the same way as for ours experiments. The boundary conditions are a free-slip boundary on the lateral side of the domain, a free outflow for the top boundary and a no-slip conditions for the bottom. Due to the adaptive mesh refinement and parallelization of the model, computations for the finest mesh last around 4 hr on 4 processors (Intel Xeon 2.80 GHz)

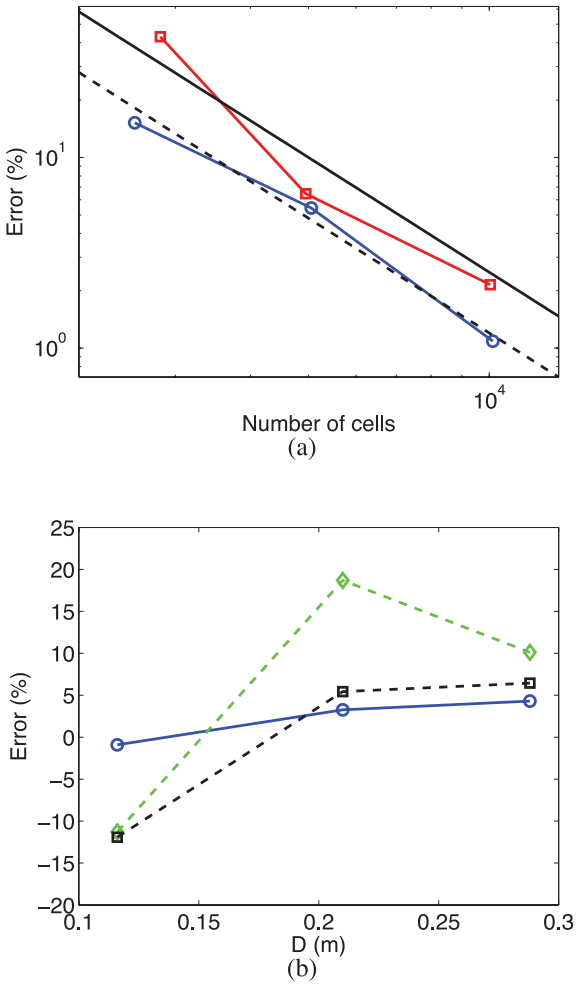

Figure A2. (a) Convergence of the error on the amplitude (Error $= |A_{\text{exp}} - A_{\text{num}}|/A_{\text{exp}}$) as a function of the spatial resolution. $D = 0.21$ m (°), $D = 0.288$ m (□) (see Table A1). Dashed and solid black lines represent the slope in N^{-2}, with N the number of cells. (b) Comparison of the error on the amplitude between Gerris (□), Monaghan & Kos (2000) (°) and Abadie *et al.* (2010) (◇). Numerical results are in good agreement with experiments and previous numerical simulations.

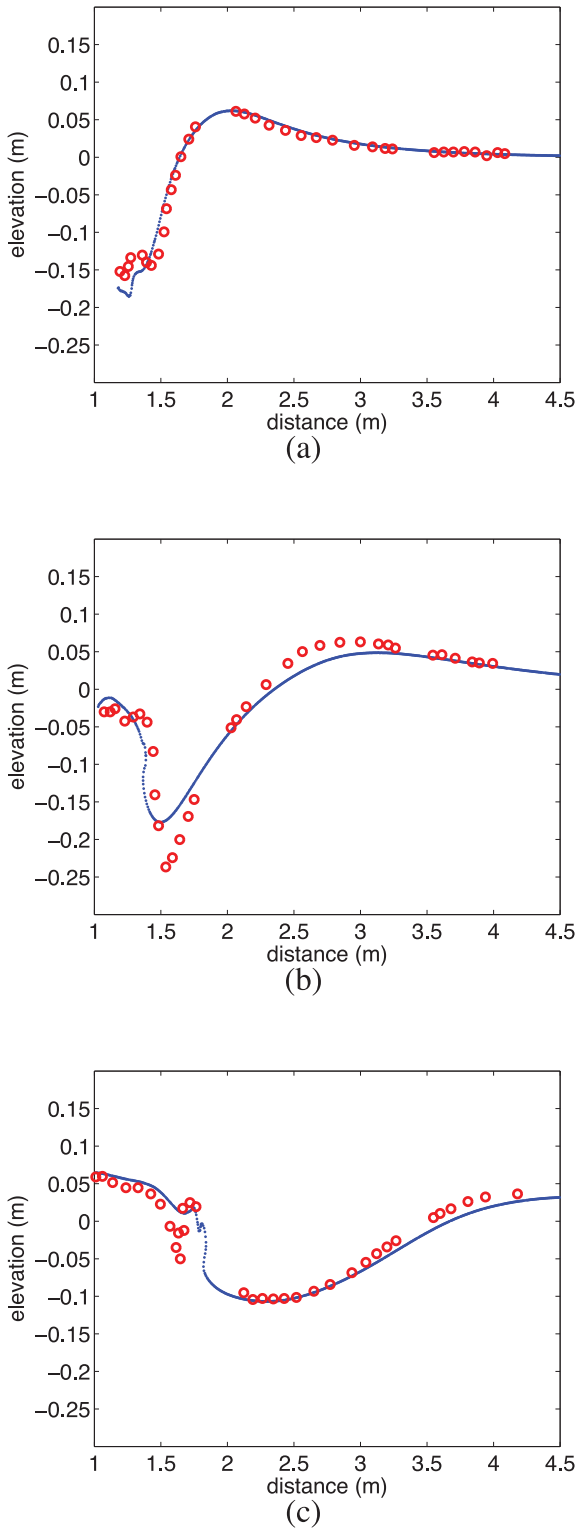

Figure B1. Comparison between numerical and experimental wave profiles (from left to right) at $t = 0.5$, 1 and 1.5 s. Heinrich's experiments (◯), Gerris (solid line). Computed free surface is in very good agreement with the experiment.

and only 10 min for the coarsest mesh. We only simulate 1 s of the experiment, which is long enough to allow the wave to reach the probe. The use of a finer grid improves the accuracy of the results on the wave amplitude except for the lowest water depth. Fig. A2 shows the adaptive convergence results for the water depth $D =$ 0.21 and 0.288 m. The number of cells for the three refinements is calculated when the maximum amplitude reach the probe. The maximum amplitude arrival time at the probe can vary from about 0.02 s depending on the refinement. Consistent convergence is obtained and is very close to a second-order convergence with the number of cells (dashed and solid black curve in Fig. A2a). Numerical errors between our results and those of Monaghan & Kos (2000) and Abadie *et al.* (2010) are compared for the three water depths (Fig. A2b). The experimental results are chosen as reference. The refinement level is set equal to 7 (our smallest cell edge is then about 7 mm), which is a good trade-off between accuracy and computational time (see Table A1). Our simulations are in good agreement with experiments. The maximum relative error with the measured wave heights is 12 per cent, which is comparable to the experimental error (20 per cent for the lowest water depth).

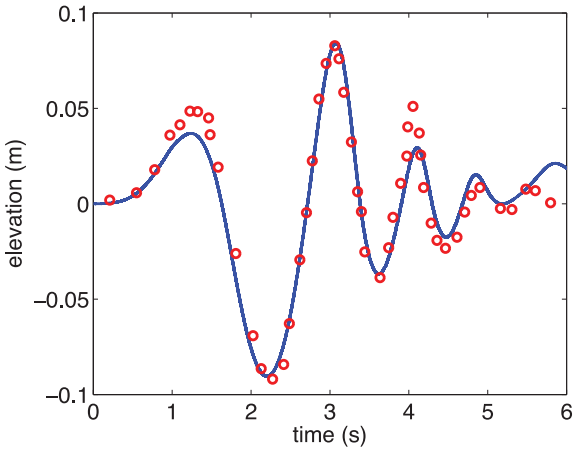

Figure B2. Comparison between Heinrich's experiment and numerical simulation at probe located at 4 m from the left end of the tank. Heinrich's experiments (◯), Gerris (solid line).

APPENDIX B: HEINRICH EXPERIMENTS

The experiment consists of a triangular (0.5 m × 0.5 m in cross-section) rigid block sliding down a 45° slope. The water depth was 1 m and the top of the block was initially located 1 cm below the free surface. A 35 mm camera was used to follow the free-surface evolution as a function of time. Three electrical contact-type gauges were used to measure the wave heights at 4, 8 and 12 m. In our simulation, the domain corresponds to a 8 m × 8 m square, so comparison with the experiment is only available for the first gauge, the second one being too close to the wall where reflection occurs very soon. Heinrich (1992) used two other gauges along the flume width at $X = 4$ m, located at 10 cm from both walls. With these gauges he confirmed that, at this location, the experiment was unidimensional along the flume width. Our numerical results are compared to Heinrich's experiments. Here again we used the real value of density and viscosity, so the solver is tuned in the same way as for the Russell's wave generator simulations (Section A). The maximum refinement level is 10, which gives a smallest cell edge of $8/2^{10} \approx 8$ mm. The boundary conditions for this simulation are the same as Section 2.2 (see this section for further details). The computation time for this configuration is about 1.5 hr on one processor (Intel Xeon 2.80 GHz). In Fig. B1 is shown a comparison between the computed and experimental wave profiles at $t = 0.5$, 1 and 1.5 s. We can observe that the overall behaviour of the free-surface displacement is in good agreement with the experiment. At $t = 0.5$ s, discrepancies occur near the solid. This has also been observed in earlier simulations (Heinrich 1992; Abadie *et al.* 2010) and can be explained by the highly turbulent motions near the solid. At $t = 1$ s, we observe the same phenomenon near the slide where the simulated trough is smaller than the experiment. At $t = 1.5$ s a slight plunging breaker is observed in the simulation. For all the cases in the propagation regime, our numerical results are in very good agreement with the experiment. Fig. B2 demonstrates this overall good agreement, comparing the time evolution of the free-surface elevation at the first gauge during the first 6 s. The first small crest is slightly underestimated in the simulation whereas the following trough and the highest crest are correctly reproduced. In the dispersive region, the amplitude of the crest is slightly underpredicted by the model (at $t = 4$ s) but the trough is still correctly modeled.

The validation cases presented above show that Gerris can accurately reproduce the free-surface evolution even for subaerial landslide cases that imply strong interaction between solid and water. The submarine simulation is in good agreement with the other examples (*http://gfs.sourceforge.net/wiki/index.php/Landslide-generated_tsunamis*) where the overall behaviour of the free-surface displacement is correctly numerically reproduced.